Technical report:

Effects of brittle off-fault damage on fault displacement

(SCEC Project 20121)

March 20, 2021

Investigators:

Christine Goulet[1]
Yongfei Wang[1]
Steven Day[2]

Institutional Affiliations:

[1]Southern California Earthquake Center
University of Southern California
3651 Trousdale Parkway #169
Los Angeles, CA 90089-0742

[2]Department of Geological Sciences
San Diego State University
5500 Campanile Dr
San Diego, CA 92182-1020

Abstract
Fault displacement in the near surface presents a serious potential hazard for structures and lifelines. However, fault displacement models are sparse and poorly constrained due to limited observational data. We are using physics-based simulation models that incorporate near-fault physical properties as an alternative and supplemental approach for quantifying fault displacement in seismic hazard analyses. Fault zones are complex structures exhibiting nonlinear behavior, and that is reflected in the observed displacements in the near surface. While the commonly used Drucker-Prager (DP) plasticity model accounting for the inelasticity is computationally efficient and useful to model first-order large-scale inelastic deformations, it misses numerous realistic attributes of earth materials properties and behavior. We implemented a new brittle off-fault damage model that accounts for 1) dynamic microfracture generations and 2) dynamically evolving bulk moduli. We added these selected constitutive laws into the generalized finite difference dynamic rupture simulation code (SORD). Preliminary simulation results for a simplified 2D in-plane scenario demonstrates that the brittle damage model radiates high-frequency (HF) near-fault ground motion and dynamically affects the shear wave velocity. The inelastic concentration area of the new developed damage model is similar to that predicted by the DP model, but the model provides the desired benefit of increased HF seismic radiation. Future work extending the implementation for 3D problems will make the model amenable to calibration and validation against observed data.

Introduction, Motivation, and Previous Work
Coseismic fault displacements in large earthquakes have caused significant damage to structures and lifelines (e.g., severely destroyed bridges, dams and tunnels in the 1999 Chi-Chi earthquake, collapsed buildings in the 1999 Kocaeli earthquake, damaged railroads in the 1975 Guatemala earthquake) on and near fault traces. Fault displacements pose a risk to distributed infrastructures (SCEC5 Theme) such as gas and water distribution systems, that due to their nature can not simply avoid all fault traces.

Compared to well-developed empirical ground-motion models (GMMs, a.k.a. GMPEs), empirical fault displacement models are sparse and poorly constrained partly due to the paucity of detailed high-resolution fault-displacement observations (e.g., Petersen et al., 2011; Wells and Coppersmith, 1994; Youngs et al., 2003), even despite recent large database building efforts (e.g., Baize et al., 2020; Sarmiento et al., 2019). Recent advancements in aerial imaging have allowed the observation of near-field fault deformation at a higher resolution than previously possible (e.g., Milliner et al., 2015; Milliner et al., 2016; Barnhart et al., 2020). These observations are still too sparse to completely support probabilistic fault displacement hazard analysis (PFDHA) model development, but they provide observational constraints against which simulation-based models can be validated. Physics-based simulations such as rupture dynamic models represent an attractive tool to address this important problem. These numerical simulations construct spontaneously evolving earthquake ruptures under mechanical conditions (e.g., fault geometry, friction law, stress condition and surrounding earth medium), resulting in physically plausible mechanical fault behavior and, consequently, displacements. Once validated against well-documented case histories, these dynamic rupture models can be used to predict displacements for scenarios and events we have not yet experienced. Those synthetic displacement datasets can in turn be used alone or combined with empirical observations to support PFDHA model development.

The fundamental physical attributes of a fault zone should be implemented to model realistic fault displacement profiles. During repetitive earthquake cycles, fault zones are shaped into a complex system consisting of a fine-grained narrow fault core surrounded by pervasively fractured rocks (Sibson, 1977; Chester et al., 1993; Biegel and Sammis, 2004). High stresses associated with the coseismic breakdown zone tend to be much larger than the ambient tectonic stress and even beyond what host rocks can elastically sustain (Brace et al., 1966; Scholz, 1968). Within this area, rocks are greatly damaged with multi-scale fractures (from fault branches and segments to localized microfractures) and show a significant drop in velocity compared to outer host rocks (e.g., Fialko et al., 2002; Ben-Zion et al., 2003;

Cochran et al., 2009). These attributes of observed fault zones are believed to be related to inelastic processes occuring during the earthquake rupture.

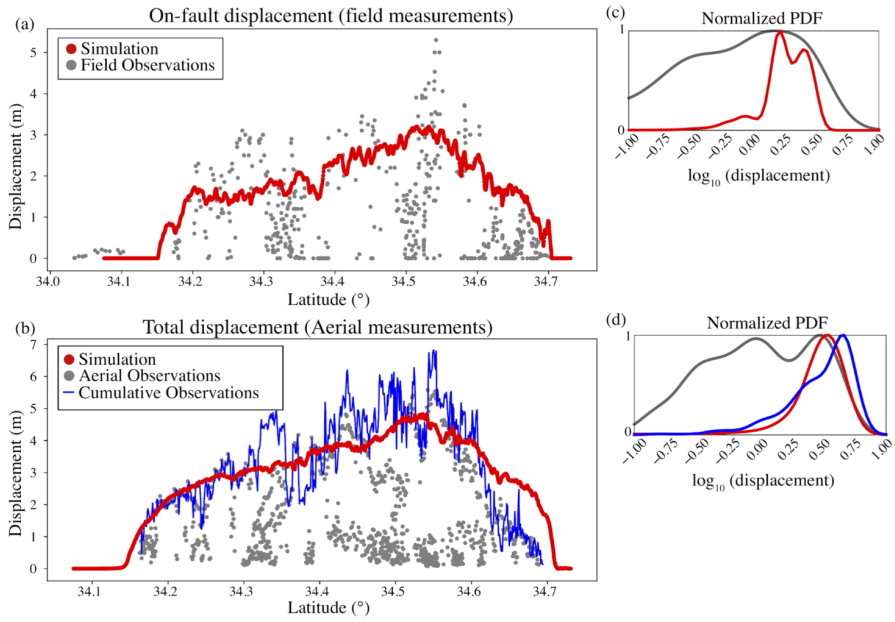

Figure 1. (a) Simulated on-fault displacement and comparison with field mapping. (b) Simulated total displacement and comparison with aerial mapping. A cumulative displacement from the aerial mapping (blue curve) is superimposed. Normalized probability density function of observations and simulations in (a) and (b) are plotted in (c) and (d), respectively. The legends in (c) and (d) are consistent with those (a) and (b).

Various model-based studies have highlighted the significant role played by inelasticity in earthquake dynamics, seismic radiation and fault displacement (Bhat et al., 2012; Lyakhovsky and Ben-Zion, 2014; Roten et al., 2017; Wang and Day, 2020). One of the most frequently used models for simulating earthquakes and seismic wave propagation is based on the Drucker-Prager (DP) plastic yield. Roten et al. (2017) used the DP criterion to model the ground deformation and found that the presence of off-fault displacements (in magnitude comparable to on-fault displacements) and shallow slip deficit (smaller slip at shallow depth) systematically observed following the 1992 Landers (Milliner et al., 2015) is likely to be a consequence of the off-fault inelasticity.

While the simplified DP is computationally efficient and useful to model a first-order large-scale inelastic deformation, it misses numerous attributes of realistic earth materials such as small-scale features and dynamically modified moduli. For example, we modeled the fault displacement from the well-documented 1992 Landers earthquake using the DP model and we reproduced the large-scale fault-displacement characteristics to a first-order degree. As shown in Figure 1, the simulated on-fault (Figure 1a) and total displacements (Figure 1b) show a good agreement with observations in the global distributions of the peak displacements. For a more quantitative comparison, the normalized probability density functions (PDF) of the simulation well capture large-scale statistical features (i.e., shapes and mean values) of on-fault (Figure 1c) and total fault displacements (Figure 1d). However, the along-strike variability of the observed fault displacements are much greater than those predicted by the simulation based on the DP model. This is also reflected in the PDFs, where our simulation have very low contributions in the small-scale fault displacements, implying that the simplified DP model can not replicate the complex patterns in part controlled by structural complexities (Milliner et al., 2015) and shallow fault discontinuities (Oglesby, 2020).

We therefore extend our modeling to include brittle damage as an improvement over the aforementioned plasticity model. In this work, we implement a brittle off-fault damage model (Bhat et al., 2012; Thomas and Bhat, 2018) accounting for dynamic off-fault microfracture generation as a proxy for off-fault inelasticity into the pre-existing dynamic rupture platform Support Operator Rupture Dynamics (SORD, Ely et al., 2009; Shi and Day, 2013; Wang and Day, 2020). The brittle damage model implemented here is featured by the characteristics: 1)

dynamically generated microfractures boosting HF seismic radiation and 2) dynamically evolving bulk properties shaping the fault zone.

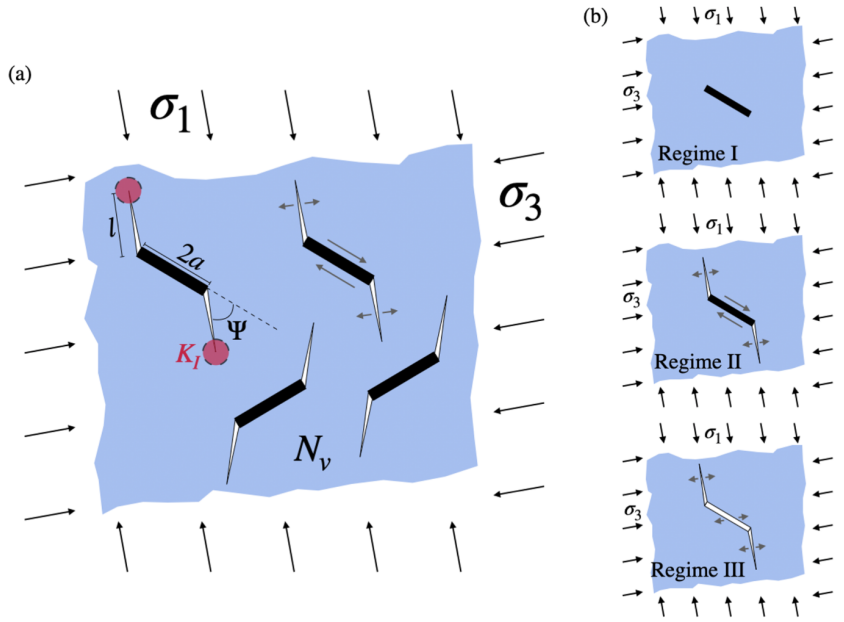

Figure 2. (a) Geometry of the micromechanical brittle damage model. Sliding on an array of penny-shaped cracks having volume density of N_v *and radius* a *produces a wedging force that drives tensile wing cracks to open in the direction of the smallest principal stress* σ_3 *and propagate along the largest principal stress* σ_1*.* K_I *is the mode-I stress intensity factor caused by the wing cracks.* Ψ *is the orientation of the penny-shaped cracks relative to* σ_1*. Gray arrows show the moving directions.* l *is the length of the wing crack. (b) Mode of inelastic deformation depending on the regime reached during the simulation.*

Implementation of the brittle damage model

Let us briefly introduce concepts of the implemented brittle damage model based on the work of Bhat et al. (2012) and Thomas and Bhat (2018). Given that tensile cracks induced by grain-boundary sliding are a major source of inelastic deformation (Bhat et al., 2012), the brittle damage model is based on the growth and interaction of tensile "wing cracks" nucleated at the tips of an initial distribution of micro-cracks as shown in Figure 2a. The pre-existing flaws in the medium are assumed as penny-shaped (i.e., disk-shaped) cracks of radius a and the volume density of the crack is Nv. Thus, the density of the initial flaws per unit volume is characterized by a scalar D_0 defined as:

$$D_0 = \frac{4\pi}{3} N_v (a\cos\Psi)^2 \qquad (1)$$

where $a\cos\Psi$ is the projection of the crack radius parallel to the largest principal stress σ_1.

Under loading, there are three regimes dependent on the local stress (Figure 2b): **Regime I** when stress is not high enough to allow sliding on the initial flaw, **Regime II** when the shear stress overcomes the frictional resistance over the flawed surface and inelastic deformation is then activated by growing tensile wing cracks, and **Regime III** when the state of stress turns tensile and both cracks and wing cracks can open. Given our assumed globally compressive stress state during earthquakes, we ignore the Regime III in our simulation. During the inelastic Regime II, the wing cracks grow along the σ_1 axis from zero to the current scale of l. Thus, the current inelastic state similar to the previously defined scalar is defined as:

$$D = \frac{4\pi}{3} N_v (a\cos\Psi + l)^2 \qquad (2)$$

Here D approaching 1 corresponds to the coalescence stage that leads to macroscopic fracturing of the solid. We can use the non-linear ordinary differential equation (see derivation in Bhat et al., 2012) to solve the state scalar D at time t:

$$\frac{dD}{dt} = \left(\frac{3D^{2/3}D_0^{1/3}}{a\cos\Psi}\right)\frac{dl}{dt} \qquad (3)$$

where $\frac{dl}{dt} \equiv v$ effectively corresponds to the instantaneous wing-crack tip speed. We numerically solve this equation with a second-order Runge-Kutta scheme (consistent with the temporal accuracy of SORD):

$$D_{n+1} = D_n + \frac{\Delta t}{2}\left(\frac{3D_n^{2/3} D_0^{1/3}}{a\cos\Psi} v_n + \frac{3(D_n + \frac{3D_n^{2/3} D_0^{1/3} v_n \Delta t}{a\cos\Psi})^{2/3} D_0^{1/3}}{a\cos\Psi} v_n \right) \quad (4)$$

where the subscript n represents the time step.

To update the state scalar, we need the instantaneous crack speed at each time step, which is obtained by Bhat et al., 2012 to balance the wing-crack stress intensity factor and its critical fracture toughness of the material for both initiation and growth. The balance is defined by the equation:

$$K_I \left\{ \frac{(1 - v/C_R)}{\sqrt{1 - v/C_p}} \right\} = K_{IC}^{SS} \left\{ \frac{1 + (v/v_m)^5}{\sqrt{1 - c/c_p}} \right\} \quad (5)$$

where C_R and C_p are Rayleigh and P wave speed, v_m is called the branching speed (a material attribute), K_I is the quasi-static stress intensity factor of an equivalent crack of the same length but growing at zero speed (computed in the simulation), and K_{IC}^{SS} is the quasi-static fracture toughness (material attribute that can be measured through laboratory experiments). We use a hybrid method to increase the efficiency of searching for the root: we first use the bisection for three iterations to find an optimal root guess that is subsequently used for the Newton-Raphson method. Generally, in our simulation, this hybrid method only takes a maximum of seven iterations to converge with a relative error of 1‰ of Rayleigh wave speed.

Finally, once we know the state scalar D_n at a certain time step and the current strain field, we solve for the stress field using the damage constitutive law:

$$\sigma_{ij} = \frac{\mu}{\Gamma}\left\{ \left(\frac{3(1-2\nu)}{1+\nu} + A_1^2 - \frac{A_1 B_1 \epsilon}{\gamma} \right)\epsilon_{ij} + \left(\frac{3\nu}{1+\nu} + \frac{B_1^2}{2} - \frac{A_1^2}{3} + \frac{A_1 B_1 \epsilon}{3\gamma} \right)\epsilon\delta_{ij} - \left(\frac{A_1 B_1}{2} \right)\gamma\delta_{ij} \right\} \quad (6)$$

where Γ is defined as $\Gamma = \left\{ \frac{3(1-2\nu)}{2(1+\nu)} + \frac{3(1-2\nu)B_1^2}{4(1+\nu)} + \frac{A_1^2}{2} \right\}$ A_1 and B_1 are functions of D (more details provided in the supplement of Thomas and Bhat, 2018), $\boldsymbol{\epsilon}$ and $\boldsymbol{\gamma}$ are related to the strain field, and ν is the Poisson's ratio.

Preliminary simulation results

For simplicity, we start with a 2D in-plane scenario. We apply uniform background stresses with the maximum compressive stress $\boldsymbol{\sigma_1}$ with an angle of 45° relative to the fault plane. Initial normal and shear stresses on the fault were set to 60.7 and 19.9 MPa, respectively. A uniform half-space velocity structure was also defined with (Vp=5600 m/s, Vs=3120 m/s, and ρ=2700kg/m^3. Rupture propagation along the fault plane is governed by a slip-weakening law in which the static friction coefficient is set 0.6, the dynamic friction coefficient is set to 0.1, and the critical slip distance is set to 1 m. Using these parameters, we follow Day et al. (2005) and estimate the static cohesive zone size to about 1054 m. For the brittle damage model, we imposed uniformly distributed pre-existing cracks with a radius of 60 m, a volume density of 1.68×10^{-7} m^{-3}, and an orientation of 29.5° relative to $\boldsymbol{\sigma_1}$, thus resulting in an initial state scalar D_0 of 0.1. Nucleation is obtained by imposing a shear traction perturbation with radius of 2 km. Spatial discretization is constrained by two length scales: cohesive zone size (~1 km) and pre-existing crack size (60 m). We follow Bhat et al. (2012) to select a discretization smaller than the crack size (20 m) and use a time step of 0.0016 s.

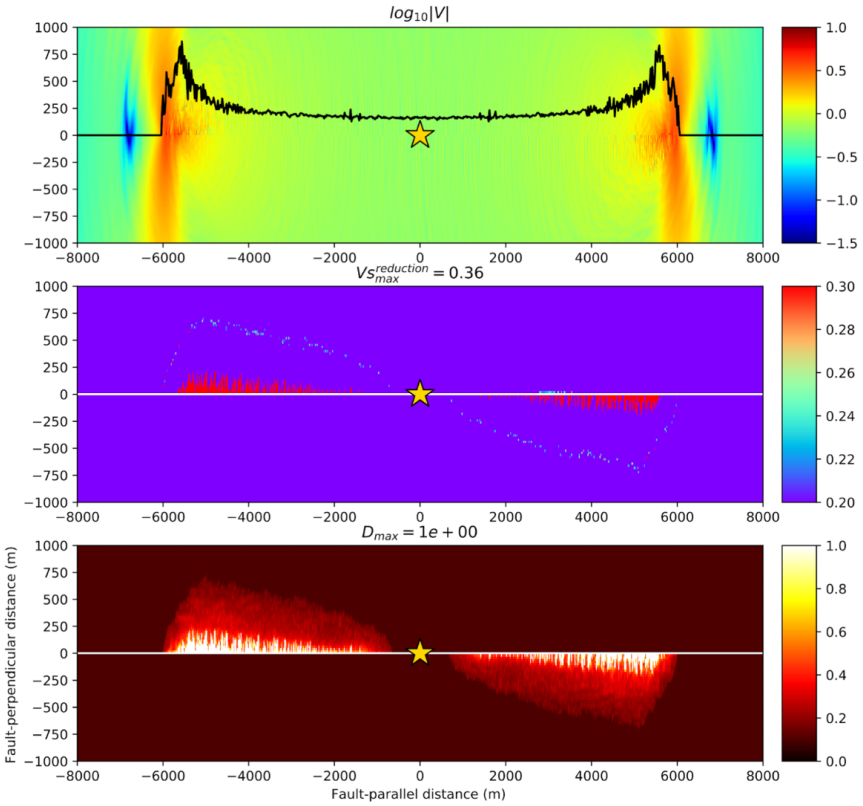

Figure 3. Snapshot of dynamic rupture simulations that include the new brittle model implementation showing various metrics along the linear fault plane in a plan view, with the hypocenter shown by the yellow star. Top: magnitude of velocity (m/s, in a logarithmic scale), black curve is the slip rate function at the selected time step. Middle: reduction ratio of shear wave speed (in per cent). Bottom: damage state scalar (D), D approaching 1 corresponds to the coalescence stage that leads to the macroscopic feature of the solid while D approaching 0 corresponds to an undamaged solid.

Figure 3 shows snapshots of velocity magnitude, reduction ratio of the shear wave speed and the damage state scalar. As we described before, the brittle damage model enriches HF seismic radiation in a near-fault regime (nearly < 1 km), as shown in Figure 3 (top). The slip rate function is under much perturbation by the brittle damage model. The maximum reduction of shear wave speed is 36% compared to the host rock, which is within the estimated range of the San Andreas Fault at Parkfield (30~40%, Li et al., 2004). In addition,the brittle damage is all in the extensional quadrant in the scenario of the maximum principal stress tilting with 45° to the fault, which is similar to the DP model (e.g., Templeton and Rice, 2008).

Summary and future work

In this study, we implement the brittle damage model in our generalized finite difference rupture dynamics code, SORD. We designed a new SORD-adaptable updating scheme for the damage state scalar D and a hybrid solution-searching scheme for the instantaneous crack tip speed v_m. The preliminary simulations demonstrate that the brittle damage model radiates HF near-fault ground motions. The ground deformation mixed with the damage state scalar as a proxy of off-fault microfracture density deserves a closer look in a future study. As shown in our plasticity-based Landers simulation, a realistic ground deformation for a strike-slip requires a 3D scenario with a mixed rupture mode (in plane and anti plane) because a pure in plane scenario cannot accommodate deformation caused by inelasticity-induced shallow slip deficit. Therefore, in future work, we will extend our simulation to a full 3D scenario with the addition of more realistic models such as depth-variable stresses and velocity structures. Future work will also involve the validation of the enriched HF near-fault ground motions against observed near-fault ground motions and results from GMMs.

References

Baize, S., et al. (2020), A Worldwide and Unified Database of Surface Ruptures (SURE) for Fault Displacement Hazard Analyses, Seismological Research Letters, 91(1), 499-520, https://doi.org/10.1785/0220190144

Barnhart, W. D., Gold, R. D., and Hollingsworth, J. (2020), Localized fault-zone dilatancy and surface inelasticity of the 2019 Ridgecrest earthquakes, Nature Geoscience, https://doi.org/10.1038/s41561-020-0628-8

Ben-Zion, Y., et al. (2003), A shallow fault-zone structure illuminated by trapped waves in the Karadere-Duzce branch of the North Anatolian Fault, western Turkey, Geophysical Journal International, 152(3), 699-717, https://doi.org/10.1046/j.1365-246X.2003.01870.x

Bhat, H. S., Rosakis, A. J., and Sammis, C. G. (2012), A Micromechanics Based Constitutive Model for Brittle Failure at High Strain Rates, Journal of Applied Mechanics-Transactions of the Asme, 79(3), 031016, https://doi.org/10.1115/1.4005897

Biegel, R. L., and Sammis, C. G. (2004), Relating fault mechanics to fault zone structure, Advances in Geophysics, Vol 47, 47, 65-111, https://doi.org/10.1016/s0065-2687(04)47002-2

Brace, W. F., Paulding, B. W., and Scholz, C. (1966), Dilatancy in the fracture of crystalline rocks, Journal of Geophysical Research, 71(16), 3939-&, https://doi.org/10.1029/JZ071i016p03939

Chester, F. M., Evans, J. P., and Biegel, R. L. (1993), Internal Structure and Weakening Mechanisms of the San-Andreas Fault, Journal of Geophysical Research-Solid Earth, 98(B1), 771-786, https://doi.org/10.1029/92jb01866

Cochran, E. S., Li, Y.-G., Shearer, P. M., Barbot, S., Fialko, Y., and Vidale, J. E. (2009), Seismic and geodetic evidence for extensive, long-lived fault damage zones, Geology, 37(4), 315-318, https://doi.org/10.1130/g25306a.1

Goulet, C., Y. Wang, C. Nweke, B. Tang, P. Wang, K. Hudson, S. Andi, X. Meng, M. Hudson, A. Donnellan, G. Lyzenga, S. Brandenberg, J. P. Stewart, T. Gallien, M. Winters, M.-P. Delisle, J. Lucey, and Y. Kim. (2021), Comparison of Surface Fault Displacement Interpretations from Field and Aerial Data for the M 6.4 and 7.1 2019 Ridgecrest Earthquake Ruptures, Bulletin of the Seismological Society of America, *in revision*

Ely, G. P., Day, S. M., and Minster, J.-B. (2009), A support-operator method for 3-D rupture dynamics, Geophysical Journal International, 177(3), 1140-1150, https://doi.org/10.1111/j.1365-246X.2009.04117.x

Fialko, Y., Sandwell, D., Agnew, D., Simons, M., Shearer, P., and Minster, B. (2002), Deformation on nearby faults induced by the 1999 Hector Mine earthquake, Science, 297(5588), 1858-1862, https://doi.org/10.1126/science.1074671

Li, Y. G., Vidale, J. E., and Cochran, E. S. (2004), Low-velocity damaged structure of the San Andreas Fault at Parkfield from fault zone trapped waves, Geophysical Research Letters, 31(12), L12s06, https://doi.org/10.1029/2003gl019044

Lyakhovsky, V., and Ben-Zion, Y. (2014), A Continuum Damage-Breakage Faulting Model and Solid-Granular Transitions, Pure and Applied Geophysics, 171(11), 3099-3123, https://doi.org/10.1007/s00024-014-0845-4

Milliner, C. W. D., Dolan, J. F., Hollingsworth, J., Leprince, S., and Ayoub, F. (2016), Comparison of coseismic near-field and off-fault surface deformation patterns of the 1992 M-w 7.3 Landers and 1999 M-w 7.1 Hector Mine earthquakes: Implications for controls on the distribution of surface strain, Geophysical Research Letters, 43(19), 10115-10124, https://doi.org/10.1002/2016gl069841

Milliner, C. W. D., Dolan, J. F., Hollingsworth, J., Leprince, S., Ayoub, F., and Sammis, C. G. (2015), Quantifying near-field and off-fault deformation patterns of the 1992 M-w 7.3 Landers earthquake, Geochemistry Geophysics Geosystems, 16(5), 1577-1598, https://doi.org/10.1002/2014gc005693

Oglesby, D. D. (2020), What Can Surface-Slip Distributions Tell Us about Fault Connectivity at Depth? Bulletin of the Seismological Society of America, https://doi.org/10.1785/0120190245

Petersen, M. D., Dawson, T. E., Chen, R., Cao, T. Q., Wills, C. J., Schwartz, D. P., and Frankel, A. D. (2011), Fault Displacement Hazard for Strike-Slip Faults, Bulletin of the Seismological Society of America, 101(2), 805-825, https://doi.org/10.1785/0120100035

Roten, D., Olsen, K. B., and Day, S. M. (2017), Off-fault deformations and shallow slip deficit from dynamic rupture simulations with fault zone plasticity, Geophysical Research Letters, 44(15), 7733-7742, https://doi.org/10.1002/2017gl074323

Sarmiento, A., et al. (2019), A New Model Database for Next-Generation Fault Displacement Hazard Analysis, Seismological Society of America Annual Meeting, Seattle

Savage, H. M., and Brodsky, E. E. (2011), Collateral damage: Evolution with displacement of fracture distribution and secondary fault strands in fault damage zones, Journal of Geophysical Research-Solid Earth, 116, B03405, https://doi.org/10.1029/2010jb007665

Shi, Z., and Day, S. M. (2013), Rupture dynamics and ground motion from 3-D rough-fault simulations, Journal of Geophysical Research-Solid Earth, 118(3), 1122-1141, https://doi.org/10.1002/jgrb.50094

Sibson, R. H. (1977), Fault rocks and fault mechanisms, Journal of the Geological Society, 133(3), 191-213, https://doi.org/10.1144/gsjgs.133.3.0191

Templeton, E. L., and Rice, J. R. (2008), Off-fault plasticity and earthquake rupture dynamics: 1. Dry materials or neglect of fluid pressure changes, Journal of Geophysical Research-Solid Earth, 113(B9), B09306, https://doi.org/10.1029/2007jb005529

Thomas, M. Y., and Bhat, H. S. (2018), Dynamic evolution of off-fault medium during an earthquake: a micromechanics-based model, Geophysical Journal International, 214(2), 1267-1280, https://doi.org/10.1093/gji/ggy129

Vermilye, J. M., and Scholz, C. H. (1998), The process zone: A microstructural view of fault growth, Journal of Geophysical Research-Solid Earth, 103(B6), 12223-12237, https://doi.org/10.1029/98jb00957

Wang, Y., and Day, S. M. (2020), Effects of off-fault inelasticity on near-fault directivity pulses, Journal of Geophysical Research: Solid Earth, 125(7), e2019JB019074, https://doi.org/10.1029/2019JB019074

Wang, Y., and Goulet, C. (2020), Validate simulated fault displacements from dynamic rupture against the observed in the 1992 Landers earthquake, Bulletin of the Seismological Society of America, *in review*

Wells, D. L., and Coppersmith, K. J. (1994), New Empirical Relationships among Magnitude, Rupture Length, Rupture Width, Rupture Area, and Surface Displacement, Bulletin of the Seismological Society of America, 84(4), 974-1002

Youngs, R. R., et al. (2003), A methodology for probabilistic fault displacement hazard analysis (PFDHA), Earthquake Spectra, 19(1), 191-219, https://doi.org/10.1193/1.1542891